

Hierarchically Porous Multimetal-Based Carbon Nanorod Hybrid as an Efficient Oxygen Catalyst for Rechargeable Zinc–Air Batteries

Dezhang Ren, Jie Ying, Meiling Xiao, Ya-Ping Deng, Jiahua Ou, Jianbing Zhu, Guihua Liu, Yi Pei, Shuang Li, Altamash M. Jauhar, Huile Jin, Shun Wang,* Dong Su, Aiping Yu, and Zhongwei Chen*

The lack of efficient strategies to address the intrinsic activity, site accessibility, and structural stability issues of metal-carbon hybrid catalysts is restricting their real-world implementation on the basis of rechargeable zinc–air batteries. Herein, a dual metal–organic frameworks (MOFs) pyrolysis strategy is developed to regulate the intrinsic activity and porous structure of the derived catalysts, where a Fe₂Ni_MIL-88@ZnCo_zeolitic imidazolate framework (ZIF), with a hierarchically porous structure, multifunctional components, and an integrated architecture, acts as an ideal precursor to obtain multimetal based porous nanorod (FeNiCo@NC-P). Benefitting from the synergetic effect of the multimetal components, facilitated reactant accessibility, and the well-retained integrated structure, the resultant FeNiCo@NC-P catalyst exhibits an oxygen reduction reaction half-wave potential of 0.84 V as well as an oxygen evolution reaction potential of 1.54 V at 10 mA cm⁻². Furthermore, the practical application of FeNiCo@NC-P in the zinc–air battery displays a low voltage gap and long-term durability (over 130 h at a current density of 10 mA cm⁻²), which outperforms the commercial noble metal benchmarks. This work not only affords a competitive bifunctional oxygen electrocatalyst for zinc–air batteries but also paves a new way to design and fabricate MOF-derived materials with tunable catalytic properties.

The overall energy efficiency of zinc–air batteries is largely determined by the air electrode reactions, oxygen reduction, and evolution reactions (ORR/OER).^[2] However, both reactions are kinetically sluggish, therefore efficient and stable bifunctional catalysts are necessitated to reduce overpotential and increase durability.^[3] Although noble metals such as Pt, Ru, and Ir exhibit high catalytic activities for ORR (Pt) and OER (Ir, Ru), their scarcity, high cost, insufficient bifunctionality, and poor durability severely restrict their widespread application.^[4] Motivated by this challenge, the development of cost-effective, robust, and durable bifunctional oxygen electrocatalysts is attracting enormous attentions.^[5]

Among the various nonprecious metal catalysts ever reported, the hybrids composed by transition-metal-based materials such as metal oxides, metal chalcogenides, and metal phosphides with heteroatom doped carbon materials,

herein named metal-heteroatom-carbon (MHC) are regarded as the most promising alternative.^[6] In the past decades, intensive efforts have been devoted to the rational design of the foregoing hybrids with the three strategies taken into consideration: i) manipulate intrinsically active sites for both ORR and OER,

1. Introduction

Zinc–air batteries possessing high theoretical energy density (1084 W h kg⁻¹), low cost, and eco-friendly are developed as a promising candidate to replace lithium-ion batteries.^[1]

Dr. D. Ren, Dr. H. Jin, Prof. S. Wang
Nano-Materials and Chemistry Key Laboratory
Institute of New Materials and Industrial Technologies
Wenzhou University
Wenzhou, Zhejiang 325035, China
E-mail: shunwang@wzu.edu.cn

Dr. D. Ren, Dr. M. Xiao, Dr. Y.-P. Deng, J. Ou, Dr. J. Zhu, Dr. G. Liu,
Dr. Y. Pei, A. M. Jauhar, Prof. A. Yu, Prof. Z. Chen
Department of Chemical Engineering
Waterloo Institute for Nanotechnology
University of Waterloo
Waterloo, Ontario N2L3G1, Canada
E-mail: zhwenchen@uwaterloo.ca

 The ORCID identification number(s) for the author(s) of this article can be found under <https://doi.org/10.1002/adfm.201908167>.

Dr. J. Ying
School of Chemical Engineering and Technology
Sun Yat-sen University
Zhuhai 519082, China

Dr. S. Li, Prof. D. Su
Center for Functional Nanomaterials
Brookhaven National Laboratory
Upton, NY 11973, USA

Prof. D. Su
Beijing National Laboratory for Condensed Matter Physics
Institute of Physics
Chinese Academy of Sciences
Beijing 100190, China

DOI: 10.1002/adfm.201908167

ii) build intimate interfacial contact between transition-metal-based materials and conductive heteroatom doped carbon to facilitate charge transfer and reduce interfacial resistance, iii) regulate porous structure to expose active sites and allow efficient diffusion of oxygen and electrolyte which could decrease the concentration polarization during catalytic oxygen reaction. In these regards, metal–organic frameworks (MOFs) are hailed as a promising class of precursor template for synthesis of MHC because of the innate porosity, tunable metals, and heteroatoms of MOF templates.^[7] Despite significant progress achieved, the singular morphology structure and limited choice of metal centers of conventional single MOF hamper the further activity improvement of the pyrolyzed MHC. Besides, compared with single metal MHC,^[8] bimetallic (Ni-Co, Ni-Fe, Fe-Co),^[9] and trimetallic (Ni-Fe-Co)^[10] catalysts were demonstrated to exhibit higher performance for oxygen catalysis due to the optimized electronic structure and enhanced charge transfer. This calls for the design of dual or multi-MOFs to progress (or pivot) toward well-regulated porosity and increased intrinsic activity from the synergetic effect of multimetal components. However, the research on this strategy for synthesizing highly effective bifunctional catalysts for zinc–air batteries is rarely reported.

Herein, we report a novel dual-MOFs pyrolysis strategy for the fabrication of a carbon nanotube (CNT)-grafted, nitrogen-doped carbon nanorod embedded with Fe-Ni-Co metal/metal phosphide nanoparticles (referred to as FeNiCo@NC-P) with a well-designed Fe₂Ni_MIL-88@ZnCo_zeolitic imidazolate framework composite (referred to as FeNi_M@ZnCo_Z) as precursors. The prepared hybrid contains many desirable features such as embedded multimetal/metal phosphide nanoparticles, nitrogen dopants, micro/mesoporous structure, large specific area, and complex morphology. To the best of our knowledge, the current hybrid nanostructure of dual-MOF-derived FeNiCo@NC-P is being reported for the first time. The optimized catalyst of FeNiCo@NC-P shows remarkable ORR and OER performance in KOH electrolyte, exhibiting an ORR half-wave potential of 0.84 V and an OER potential of 1.54 V at 10 mA cm⁻². As a practical demonstration, it exhibits a low charge–discharge

voltage gap at a current density of 10 mA cm⁻² and outstanding durability maintaining over 130 h for zinc–air battery test when serving as catalyst in an air electrode.

2. Results and Discussion

2.1. Synthesis and Physicochemical Characterizations

The synthetic strategy of FeNiCo@NC-P is illustrated in **Figure 1**. At first, Fe₂Ni_MIL-88 nanorods are prepared by a solvothermal method^[11] and then functionalized with polyvinylpyrrolidone (PVP) for absorbing organic molecules and metal ions to form ZIFs on their surfaces (Figure 1a). As shown in **Figure 2a**, the diameter of each Fe₂Ni_MIL-88 nanorod is around 100 nm, therefore, controlling the size of Co-based ZIFs below 100 nm for homogeneously covering all these rod surfaces during the crystal growth process is necessary. Deserving to be mentioned, carbonaceous material derived from small-sized Co-based ZIF is favorable for improving the specific area and exposing active sites.^[12] Hence, tuning the molar ratio of Co/Zn to adjust the size of ZIF is a suitable strategy.^[13] As shown in Figure 2b–d, the morphology of FeNi_M@ZnCo_Z undergoes drastic changes with the tuning of Co/Zn ratio. Co/Zn ratio of 1:1 gives ZIFs particles around 30–50 nm anchored uniformly on the surface of Fe₂Ni_MIL-88 rods (Figure 2b and Figure S1, Supporting Information). XRD patterns also confirm that FeNi_M@ZnCo_Z is constructed by ZnCo_ZIF and Fe₂Ni_MIL-88 (Figure S2, Supporting Information). The size of ZIFs increases obviously with the Co/Zn ratio, and when the Co/Zn ratio exceeds 1:1, the size of ZIFs is more than 500 nm, which is not fit to anchor onto Fe₂Ni_MIL-88, resulting in the synthesized ZIF polyhedrons and Fe₂Ni_MIL-88 rods being completely separated (Figure 2c,d). Additionally, physical mixture of ZnCo_ZIF and Fe₂Ni_MIL-88 rods (referred as FeNi_M/ZnCo_Z) was also prepared and cannot form a well-covered structure (Figure S3e, Supporting Information). From photographs of these MOFs,

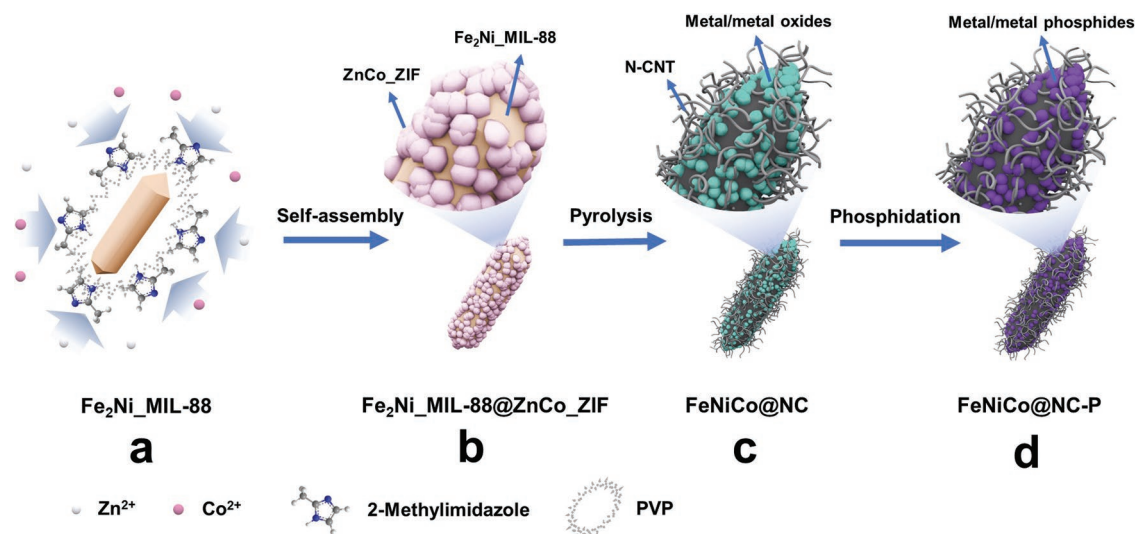


Figure 1. Illustration of synthetic strategy of FeNiCo@NC-P.

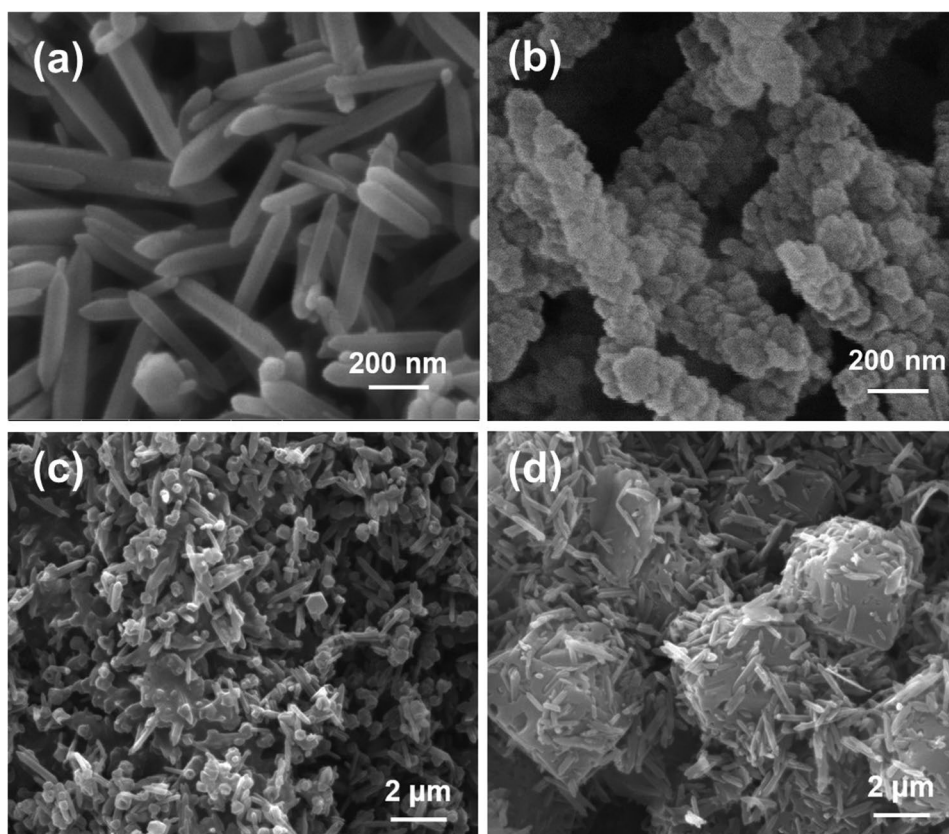


Figure 2. SEM images of a) $\text{Fe}_2\text{Ni_MIL-88}$ and as-prepared FeNi_M@ZnCo_Z with different Co/Zn ratios: b) 1:1, c) 3:1, and d) 1:0.

FeNi_M/ZnCo_Z shows dark pink color indicating the exposure of uncovered $\text{Fe}_2\text{Ni_MIL-88}$ (Figure S3a–d, Supporting Information).

Subsequently, the FeNi_M@ZnCo_Z was subject to pyrolysis of in Ar atmosphere to yield FeNiCo@NC (Figure 1c). As shown in scanning electron microscopy (SEM) and transmission electron microscope (TEM) images (Figure S4a–c, Supporting Information), the ZIFs particles anchored on MIL surface structure is completely converted into integral metal/metal oxides nanoparticles embedded within 1D carbon nanorods, with numerous tiny CNTs uniformly covering the surface of the nanorods. The in situ formed CNTs which twined on carbon nanorod can make the hybrids more stable and expose more interfaces for reaction.^[14] The coexistence of $\text{Fe}_{0.64}\text{Ni}_{0.36}$ alloy (powder diffraction file (PDF) No. 47-1405), metallic CoFe alloy (PDF No. 44-1433), and CoFe_2O_4 (PDF No. 03-0864) in FeNiCo@NC is confirmed by X-ray diffraction (XRD) (Figure S5a, Supporting Information), indicating a strong metal exchange between two MOFs during the pyrolysis. High-resolution TEM images (Figure S4d,e, Supporting Information) show that the edge of nanorod is well covered with short CNTs and metal/metal oxides nanoparticles are surrounded by graphitic carbon. This intimate contact structure ensures fast charge transfer and low interfacial resistance.^[15] High-angle annular dark field scanning transmission electron microscope (HAADF-STEM) and corresponding element mapping indicate the uniform distribution of Fe, Ni, Co, N, and C in FeNiCo@NC (Figure S4f, Supporting Information) which also confirms the strong interaction between two MOFs.

In contrast, pyrolysis of single ZnCo_ZIF , $\text{Fe}_2\text{Ni_MIL-88}$ and their physical mixture separately, which are named as Co@NC , FeNi@C , and FeNi@C/Co@NC , cannot generate CNTs, even the rod structure of FeNi@C is collapsed during the high temperature pyrolysis (Figures S3f and S6, Supporting Information). It goes to show that the covered ZnCo_ZIF maintains the rod structure of FeNiCo@NC and intimate contact between two MOFs is beneficial for enhancing interactions between elements to form an integral hybrid during the pyrolysis process.

To obtain the final FeNiCo@NC-P catalyst, the phosphidation process is carried out by treating FeNiCo@NC with NaH_2PO_2 at 300 °C in Ar (Figure 1d). In comparison, Co@NC-P , FeNi@C-P , and FeNi@C/Co@NC-P are obtained from Co@NC , FeNi@C , and FeNi@C/Co@NC via same phosphidation process. The composition of FeNiCo@NC-P is analyzed by inductively coupled plasma (ICP), and the content of Fe, Ni, Co, and Zn are 11.81, 4.03, 9.18, and 0.27 wt%, respectively. The XRD pattern (Figure S5a, Supporting Information) of FeNiCo@NC-P shows that the broad peak between 20° and 30° can be assigned to the graphitic carbon, parts of $\text{Fe}_{0.64}\text{Ni}_{0.36}$ and CoFe alloy still exist. Ni_2P (PDF No. 03-0953), FeP (PDF No. 65-2595), and CoP (PDF No. 65-1474) are also determined, suggesting a partial phosphidation. This similar transition process is also observed on FeNi@C-P (Figure S5b, Supporting Information). However, the peaks of CoP are not observed obviously in Co@NC-P (Figure S5c, Supporting Information), indicating that Co nanoparticles buried in the carbon matrix are preserved during the phosphidation process.^[16] The morphology of FeNiCo@NC-P

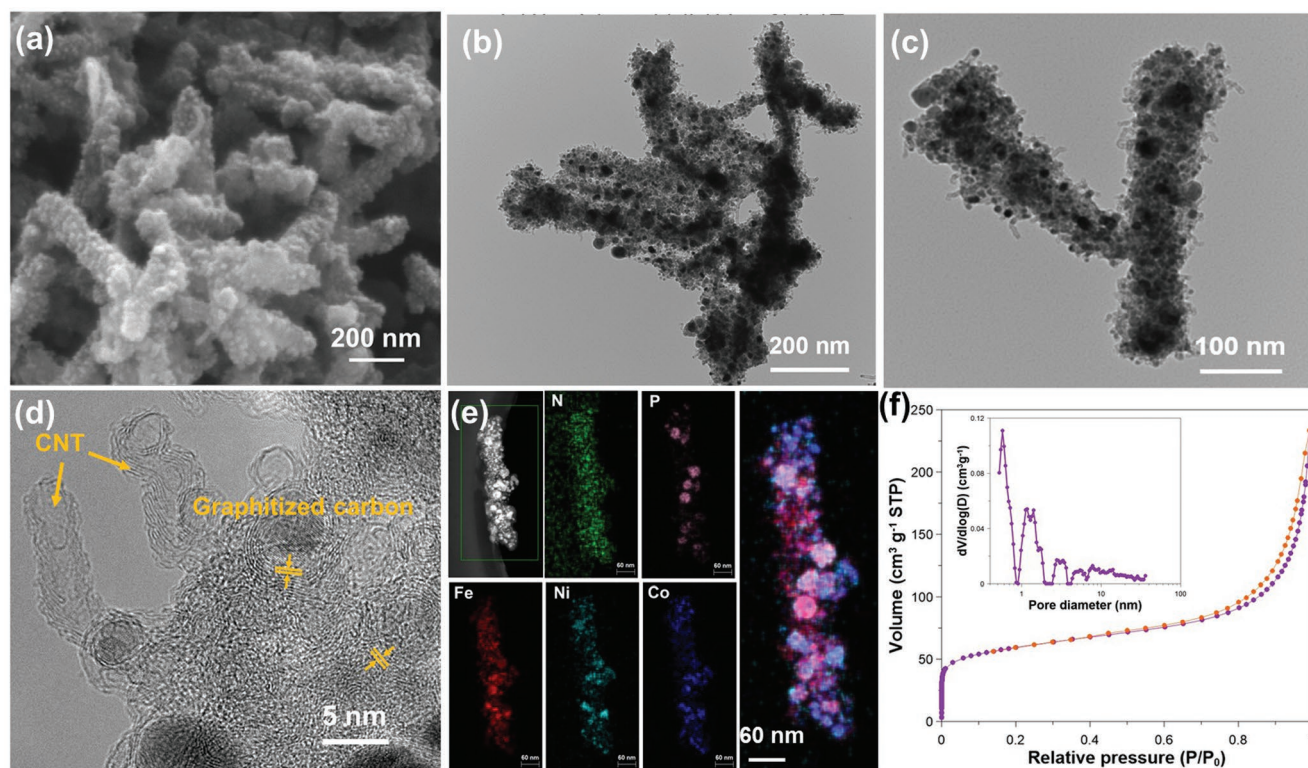


Figure 3. a) SEM image of FeNiCo@NC-P. b) Low and c) high multiple TEM images of FeNiCo@NC-P. d) High-resolution of TEM images of FeNiCo@NC-P. Yellow parallels indicate the lattice fringes of graphitic carbon. e) HAADF-STEM and element mapping of N, P, Fe, Ni, and Co of FeNiCo@NC-P. f) N_2 adsorption/desorption isotherm and pore size distribution (inset) of FeNiCo@NC-P.

with the CNTs grafted on metal-carbon rods are maintained perfectly after being treated with NaH_2PO_2 (Figure 3a–c). High-resolution TEM image shows that carbon nanorod consists of graphitic carbon (lattice spacing is around 3.4 nm) (Figure 3d), which can offer fast electron transfer to accelerate electrocatalytic process.^[5b] High-angle annular dark field STEM and corresponding element mapping result reveal that besides P, other elements such as N, Fe, Ni, and Co uniformly disperse in the carbon nanorod (Figure 3e). Higher multiple images confirm that only parts of carbon nanorod display the presence of P (Figure S7, Supporting Information). It indicates the successful N doping and partial phosphidation of catalyst. N_2 adsorption and desorption measurement was conducted to investigate the pore structure and specific surface area of FeNiCo@NC-P. As shown in Figure 3f, FeNiCo@NC-P possesses a large specific area of $200\text{ m}^2\text{ g}^{-1}$, which is larger than single MOF derived FeNi@C-P, Co@NC-P, and their physical mixture derived FeNi@C/Co@NC-P (Figure S8, Supporting Information). The isotherm displays an obvious hysteresis loop indicating the mesoporous feature of FeNiCo@NC-P. The pore size distribution shows the coexistence of micro and mesopores which guarantees plenty of active sites and efficient diffusion oxygen and electrolyte.

X-ray photoelectron spectroscopy (XPS) was conducted to understand the chemical environment and bonding configuration of FeNiCo@NC-P. High-resolution XPS profile of C 1s, N 1s, P 2p, Fe $2p_{3/2}$, Ni $2p_{3/2}$, and Co $2p_{3/2}$ is shown in Figure 4. The C 1s XPS spectrum of FeNiCo@NC-P (Figure 4a) can be

deconvoluted into four peaks for C–C/C=C (284.6 eV), C–N (285.6 eV), C–O (286.8, 286.9 eV), and O–C=O (289.0 eV).^[17] The presence of C–N confirms the N doping in FeNiCo@NC-P which is commonly considered to boost the oxygen electrocatalytic activity of carbon-based materials.^[7b,18] The peaks of N 1s XPS spectrum (Figure 4b) located at 398.5, 399.7, 400.3, 401.1, and 403.3 eV can be assigned to pyridinic-N, metal-Nx, pyrrolic N, graphitic-N, and oxidized-N, respectively.^[18,19] Over 83% of N are either pyridinic (51.0%), metal-Nx (7.1%), or graphitic-N (24.2%), where all of them are advantageous to ORR.^[20] Compared with no XPS signal of P at FeNiCo@NC, two peaks of P 2p XPS spectra of FeNiCo@NC-P (Figure 4c) located at 129.5 and 130.4 eV correspond to P $2p_{3/2}$ and P $2p_{1/2}$, which are assigned to metal-P, suggesting a successful phosphidation process. The peak at 133.6 eV represents P–O species, indicating an inevitable oxidation of the surface of metal phosphides.^[21] The Co $2p_{3/2}$ spectrum of FeNiCo@NC reveals four fitted peaks (Figure 4d) at 778.2, 780.0, 782.5, and 785.6 eV which can be assigned to the metallic Co, oxidized Co species, auger peak of Fe, and satellite peak of Co.^[22] The formation of oxidized Co species is attributed to the exposure of Co in air.^[23] According to the previous reports, Co-P covalent bonds can decrease the electron density of Co species, thus making a small shift of Co 2p spectrum.^[22a,24] As expected, the whole spectrum shifted to higher binding energy after phosphidation process. Especially, the binding energies of metallic Co and oxidized Co species in FeNiCo@NC-P shift to 778.4 and 781.0 eV, indicating the formation of Co-P and Co-PO_x, respectively.^[25]

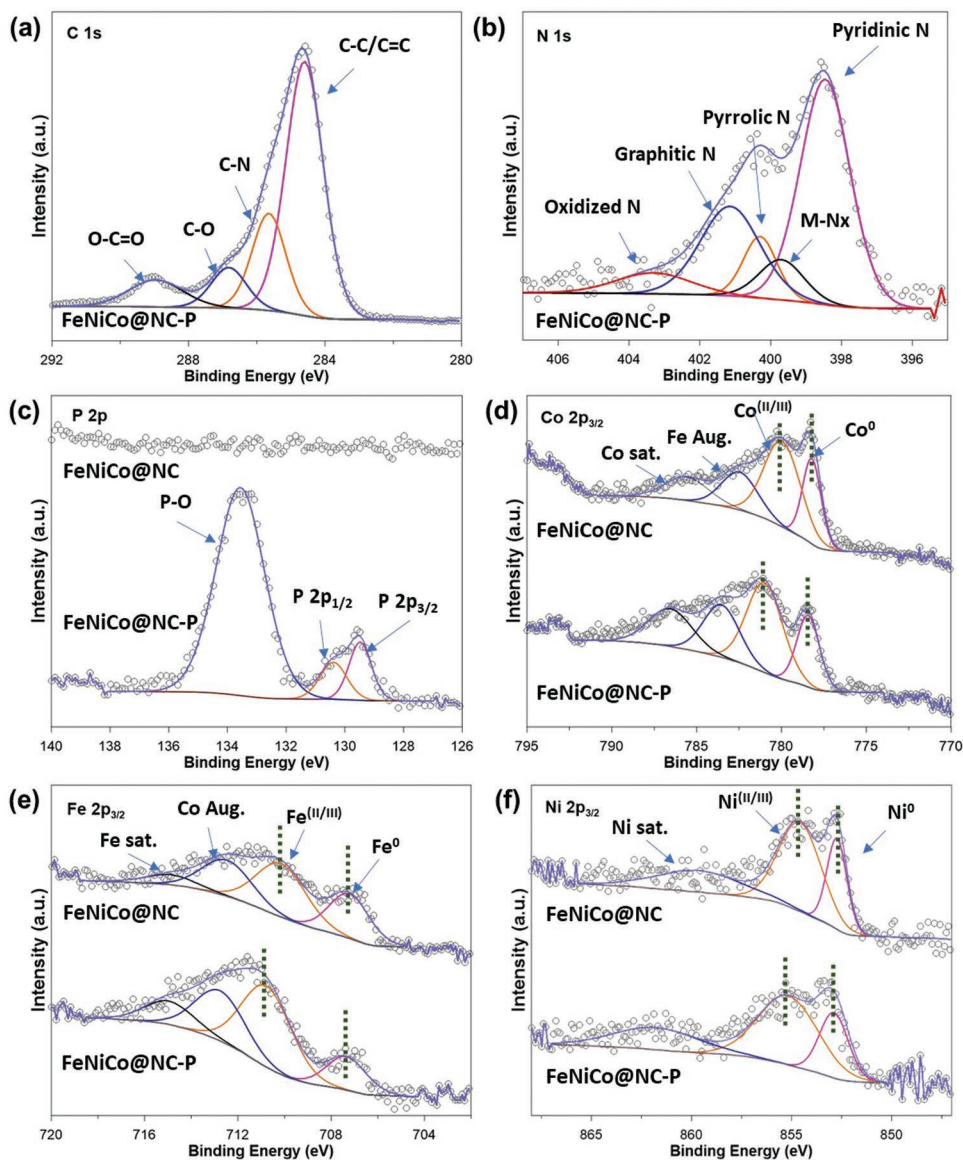


Figure 4. a) C 1s, b) N 1s, c) P 2p, d) Co $2p_{3/2}$, e) Fe $2p_{3/2}$, and f) Ni $2p_{3/2}$ XPS spectra of FeNiCo@NC and FeNiCo@NC-P.

Although the binding energy shift demonstrates the formation of CoP, the peak from FeNiCo@NC-P at 778.4 eV only shifted 0.2 eV which establishes the existence of the mixture of metallic Co and CoP.^[22a,26] Similar to the Co $2p_{3/2}$ spectrum, the deconvoluted peaks of Fe $2p_{3/2}$ spectrum of FeNiCo@NC-P (Figure 4e) at 710.8, 712.8, and 715.0 eV correspond to oxidized Fe species, Auger peak of Co, and satellite peak of Fe. The fitted peaks at 707.3 eV cannot be confirmed as Fe-P since the peaks of metallic Fe (707.2 eV) and Fe-P (707.3 eV) are very close.^[9c,27] Notably, oxide state of Fe displays an obvious positive shift of 0.7 eV from 710.1 to 710.8 eV, and the ratio increases from 39.2% to 44.5%, meanwhile metallic state of Fe decreases from 26.8% to 14.9%, indicating the metallic Fe is oxidized via H_3P to form Fe-P. Ni $2p_{3/2}$ region of FeNiCo@NC-P (Figure 4f) exhibits three fitted peaks located at 853.2, 855.7, and 861.4 eV, which can be assigned to Ni-P, oxidized Ni species, and satellite, respectively.^[9c] Compared with the binding energies of

metallic Ni and oxidized Ni species in FeNiCo@NC which are located at 852.7 and 854.5 eV, the peaks at 853.2 and 855.7 eV in FeNiCo@NC-P have a 0.5 and 1.2 eV positive shift, respectively, indicating the formation of Ni-P and Ni-PO_x.^[9c,28] The formation of partial phosphidation species contribute to constructing metal-semiconductor which is considered to be able to boost the catalytic activity.^[22a]

2.2. Electrochemical Characterizations

To assess the OER performance, the FeNiCo@NC-P was first activated by cyclic voltammetry (CV) treatment in 0.1 M KOH solution and then tested by linear scan voltammetry (LSV). Co@NC-P, FeNi@C-P, FeNi@C/Co@NC-P, and commercial Ir/C were employed for comparative study. As shown in Figure 5a, current density of 10 mA cm⁻² is achieved by

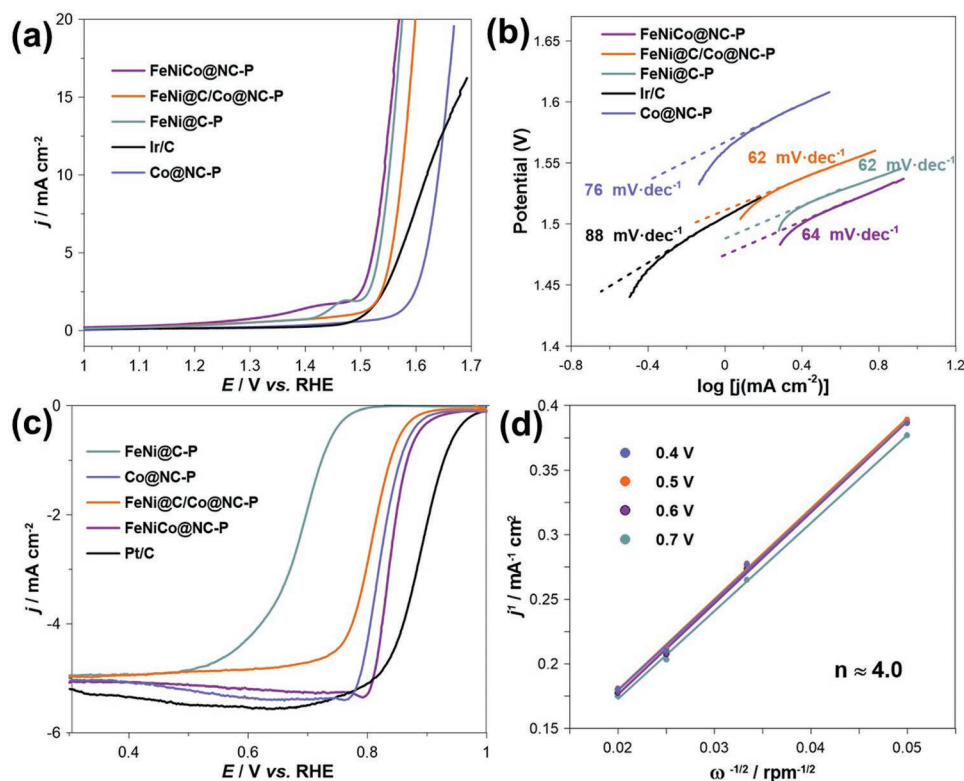


Figure 5. The OER performance of FeNiCo@NC-P, FeNi@C/Co@NC-P, FeNi@C-P, Co@NC-P, and Ir/C in N₂-saturated 0.1 M KOH solution: a) LSV curves with the rotating speed of 1600 rpm at 10 mV s⁻¹ and b) Tafel plots of the corresponding catalysts. ORR performance of FeNiCo@NC-P, FeNi@C/Co@NC-P, FeNi@C-P, Co@NC-P, and Pt/C in O₂-saturated 0.1 M KOH solution: c) LSV curves with the rotating speed of 1600 rpm at 10 mV s⁻¹ and d) K–L plots of the FeNiCo@NC-P at various potentials.

FeNiCo@NC-P at the potential of 1.54 V ($E_{j=10}$), which is the lowest potential compared to FeNi@C-P (1.55 V), FeNi@C/Co@NC-P (1.57 V), Co@NC-P (1.64 V), and benchmark Ir/C catalyst (1.62 V). Although single-MOF-derived carbon material (FeNi@C-P) also exhibits good performance for OER, there is still a gap compared with its dual-MOF-derived counterpart, which implies the importance of multimetal introduction. The slightly lower performance of FeNi@C/Co@NC-P indicates that the introduction of secondary MOFs (ZIFs) with physical blended method dilute the active sites from FeNi@C-P, which further confirms that intimate contact between two MOFs is beneficial to enhancing the multimetal synergetic effect. In addition, the poor performance of Co@NC-P is attributed that no CoP is formed and a major part of Co maintains its metallic state which cannot boost the OER activity.^[21,22] The Tafel slope of FeNiCo@NC-P (64 mV dec⁻¹), FeNi@C-P (62 mV dec⁻¹), and FeNi@C/Co@NC-P (62 mV dec⁻¹) exhibit smaller value than Co-P@NC (76 mV dec⁻¹) and commercial Ir/C (88 mV dec⁻¹), which confirms multimetal-based carbon materials possess fast OER kinetics (Figure 5b). The influence of pyrolysis temperature from 600 to 800 °C on OER performance was also investigated. As shown in Figure S9a in the Supporting Information, the catalyst annealing at 600 °C exhibits lowest OER activity with an $E_{j=10}$ value of 1.57 V, which can be attributed to its poor electronic conductivity.^[29] The reason of its poor electronic conductivity can be explained by the morphology and XRD results of FeNiCo@NC. Although the oxidized Fe, Ni, and Co

were reduced to metal and their relative alloys by carbonaceous species generated from MOFs at 600 °C, the broad XRD peaks indicating low degree of crystallization of metal and alloy, which may not catalyze carbonaceous species to form high graphitization carbon (Figure S10a, Supporting Information). Therefore, only few short in situ CNTs are observed on the rod's surface (Figure S11a, Supporting Information), which is consistent with the previous literature.^[30] Along with the rise of pyrolysis temperature (700 °C), the OER performance is improved. As expected, XRD peaks of Fe_{0.64}Ni_{0.36} and CoFe alloy in FeNiCo@NC become sharper with the increase in pyrolysis temperature (Figure S10a, Supporting Information), which may result in the formation of high graphitization carbon to boost electrochemical performances. Nevertheless, excessive temperature (800 °C) caused the obvious agglomeration of metal particles (Figure S11b, Supporting Information) which result in the decrease of the OER activity with an $E_{j=10}$ value of 1.55 V. The phosphidation process of FeNiCo@NC was also investigated by controlling the mass ratio of FeNiCo@NC and NaH₂PO₂. The transition process from metal to metal/metal phosphides hybrid can be clearly observed from XRD results (Figure S10b, Supporting Information). As shown in Figure S9b in the Supporting Information, the OER performance is improved with the increase of NaH₂PO₂ dosage, which can be ascribed to the formation and content increase of metal phosphides.

The electrocatalytic activity of FeNiCo@NC-P toward ORR was also assessed in 0.1 M KOH solution by CV and LSV. CV

curves were first obtained with N_2 and O_2 saturated electrolyte, respectively (Figure S12, Supporting Information). An obvious oxygen reduction peak at 0.78 V is observed in O_2 saturated electrolyte, and no redox peaks in N_2 saturated electrolyte, which confirms the ORR activity of FeNiCo@NC-P. As shown in Figure 5c, FeNiCo@NC-P displays superior ORR performance with half-wave potential ($E_{1/2}$) of 0.84 V, which is better than FeNi@C-P (0.68 V), Co@NC-P (0.82 V), FeNi@C/Co@NC-P (0.80 V), and comparable to commercial Pt/C (0.88 V). As expected, FeNi@C-P without coating or combining N doped carbon exhibits the lowest $E_{1/2}$. The higher ORR performance of Co@NC-P and FeNi@C/Co@NC-P against FeNi@C-P (0.68 V) indicates that the introduction of Co-based ZIF as precursor can obviously improve the ORR activity of the catalyst. Similarly for OER performance, the slightly lower performance of FeNi@C/Co@NC-P against that of Co@NC-P is also observed, which implies that the ORR active sites are mainly offered by Co@NC-P and the added Fe₂Ni_MIL-88 decreases the active sites of the mixture catalyst. These results indicate the importance of the intimate dual-MOF structure which allows the FeNiCo@NC-P to provide strong synergistic effect active sites and micro-mesoporous structure to achieve excellent ORR performance. Tafel slope of FeNiCo@NC-P (53 mV dec⁻¹) exhibits the lowest value for ORR, suggesting the fast ORR kinetics (Figure S13, Supporting Information). The influence of pyrolysis temperature on catalyst for ORR performance was also investigated and 700 °C is the optimized temperature (Figure S14a, Supporting Information). Lower temperature such as 600 °C is too low to yield high conductive precursor FeNiCo@NC as we discussed above, which led to FeNiCo@NC-P showing a poor ORR activity. TEM images and XPS results (Figures S11b and S15, Supporting Information) show that higher temperature such as 800 °C not only result in the agglomeration of nanoparticles but also reduced N content in FeNiCo@NC-P (6.44% at 600 °C; 3.80% at 700 °C; 3.11% at 800 °C). Most notable is the decrease in the ratio of pyridinic N and M-Nx to total N, which may reduce electron transfer and increase the loss of active sites.^[29] The electron transfer kinetic of ORR for FeNiCo@NC-P were further investigated by LSV at different rotation speeds ranging from 400 to 2500 rpm using rotating disk electrode (RDE, Figure S14b, Supporting Information). Koutecky–Levich (K–L) plots of FeNiCo@NC-P with good linearity and parallelism at different potentials (Figure 5d) suggest first-order reaction kinetics in relation to the concentration of dissolved oxygen.^[31] The electron transfer number derived from K–L plots is about 4.0, indicating a 4 e⁻ ORR pathway for ORR reaction.

Additionally, in order to assess the overall oxygen electrode activity of bifunctional electrocatalyst, the potential gap (ΔE) between OER potential at 10 mA cm⁻² and ORR half-wave potential metrics ($\Delta E = E_{j=10} - E_{1/2}$) was measured (Figure S16, Supporting Information). Remarkably, the FeNiCo@NC-P exhibits a ΔE value of 0.70 V which is smaller than that of commercial Pt/C and Ir/C (0.74 V), demonstrating the superior bifunctional performance of FeNiCo@NC-P. Compared with ΔE value of various transition metals, metal phosphides, and metal oxides combined with carbon based bifunctional catalysts reported in recent years, FeNiCo@NC-P also shows the lowest potential gap (Table S1, Supporting Information). The stability of FeNiCo@NC-P, FeNi@C/Co@NC-P, FeNi@C-P, Co@NC-P, and Ir/C

(Pt/C) toward OER and ORR were also evaluated. As shown in Figure S17a in the Supporting Information, FeNiCo@NC-P exhibits the best ORR durability than that of other catalysts and benchmark Pt/C. For OER durability, although the current ratio of FeNiCo@NC-P decreases obviously at first 3000 s, it still maintains about 90% of initial current after 20 000 s test, which is much better than that of benchmark Ir/C (Figure S17b, Supporting Information). In addition, rod structure of FeNiCo@NC-P and FeNi@C/Co@NC-P and particle morphology of Co@NC-P are maintained after ORR stability test, however, the morphology of FeNi@C-P is destroyed completely (Figure S18a–d, Supporting Information). For OER stability test (Figure S18e–h, Supporting Information), the rod structure of FeNiCo@NC-P and FeNi@C/Co@NC-P to some extent is cracked. The same as ORR test, the morphology of FeNi@C-P is also destroyed, while Co@NC-P maintains particle structure. The energy dispersive X-ray spectroscopy measurement was used to analyze the composition change of FeNiCo@NC-P before and after stability test (Figure S19, Supporting Information). The ratios of Fe, Ni, and Co change rarely after ORR and OER test; however, the content of P decreases obviously, illustrating the P leaching happened during the ORR and OER. Because of the excellent ORR and OER activities of FeNiCo@NC-P, a homemade rechargeable zinc–air battery was assembled using FeNiCo@NC-P as air cathode catalyst for practical applications (Figure 6a). The open-circuit voltage of the zinc–air battery with FeNiCo@NC-P is about 1.36 V (Figure S20a, Supporting Information). FeNi@C/Co@NC-P and the mixture of Pt/C and Ir/C also served as air cathode catalysts for zinc–air battery test as the reference. As illustrated in the charge/discharge polarization curves (Figure 6b), the voltage gap of charge/discharge curve for FeNiCo@NC-P increases slower than the mixture of Pt/C and Ir/C, especially at high current density. Moreover, FeNi@C/Co@NC-P shows much larger voltage gap than that of FeNiCo@NC-P, which is in agreement with their respective LSV testing (Figure S16, Supporting Information). FeNiCo@NC-P achieves a maximum power density of 112 mW cm⁻², which is much higher than that of FeNi@C/Co@NC-P (57 mW cm⁻²) and the mixture of Pt/C + Ir/C (89 mW cm⁻²) (Figure 6c). The specific capacity of the zinc–air battery with FeNiCo@NC-P is 807 mAh g⁻¹ (Figure S19b, Supporting Information).

The cycle stability tests were conducted by galvanostatic charge/discharge 1 h for each cycle at a current density of 10 mA cm⁻² (Figure 6d). It is noteworthy that zinc–air battery with FeNiCo@NC-P as catalyst achieves a small voltage gap of ≈ 0.84 V in the first 70 h, and only an additional negligible loss of 0.3 V is observed at 120 h. In contrast, the reference of Pt/C and Ir/C exhibited a large voltage gap of ≈ 1.17 V in the first 10 h and quickly degraded. Additionally, although the FeNi@C/Co@NC-P shows lower voltage gap than Pt/C and Ir/C, it is still higher than FeNiCo@NC-P. The charge voltage plateau begins to rise gradually after 70 h of testing, then an obvious increase can be observed at 80 h. Compared with other zinc–air batteries with carbon based bifunctional catalysts reported in recent years, FeNiCo@NC-P also shows excellent performance (Table S2, Supporting Information). The considerations discussed above demonstrate that intimate contact dual-MOF-derived FeNiCo@NC-P composite not only offer a superior electrocatalytic activity for zinc–air battery, but maintains a

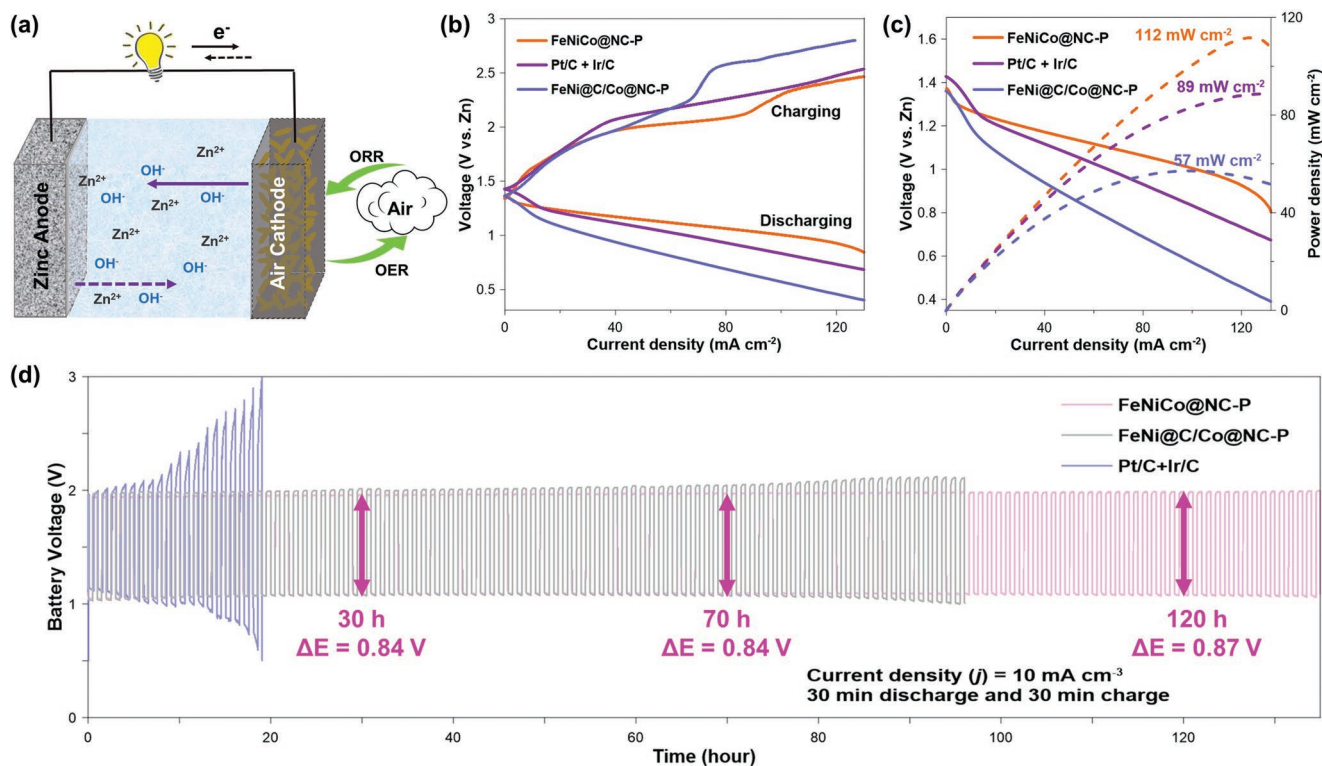


Figure 6. a) Schematic illustration of the homemade zinc–air battery. b) Charge and discharge polarization curves, c) discharge polarization curves and the corresponding power density curves, and d) cycling stability for zinc–air battery with FeNiCo@NC-P, FeNi@C/Co@NC-P and the mixture of Pt/C + Ir/C as catalysts, respectively.

longer lifetime cycling ability than that of FeNi@C/Co@NC-P and the mixture of Pt/C and Ir/C.

3. Conclusion

In summary, based on the idea for taking full advantage of different MOFs to design highly performance bifunctional oxygen catalyst for zinc–air batteries, a new strategy proposed is the organic combination of dual-MOF-hybrid ($\text{Fe}_2\text{Ni_MIL-88@ZnCo_ZIF}$) to prepare a multimetal based porous carbon nanorod composite (FeNiCo@NC-P). Compared with single-MOF-derived carbon material, the as-prepared catalyst was introduced with N dopant and multimetals including Fe, Co, and Ni. Meanwhile, micro/mesoporous structure was successfully derived from two MOF precursors and maintained 1D carbon nanorod structure after high temperature pyrolysis process. All these features guarantee FeNiCo@NC-P with highly active sites for both ORR and OER, fast charge transfer, reduced interfacial resistance, and efficient oxygen and electrolyte diffusion to display superior bifunctional ORR/OER electrocatalytic activities and excellent zinc–air battery performance. Furthermore, the organic combination of dual-MOF facilitates the N and metals exchange from different MOFs during the pyrolysis which provides more opportunities to enhance the multicomponents synergistic effect. Therefore, the FeNiCo@NC-P composite exhibited better oxygen reaction performance and longer life time of charge/discharge cycling for zinc–air battery than that of its counterpart (FeNi@C/Co@NC-P) obtained from mechanically blended $\text{Fe}_2\text{Ni_MIL-88}$ and ZnCo_ZIF . All

things considered, the present work provides a new way to design and fabricate highly active and stable bifunctional catalysts from MOF-derived composites.

4. Experimental Section

Chemicals: 2-Methylimidazole, $\text{Zn}(\text{NO}_3)_2 \cdot 6\text{H}_2\text{O}$, $\text{Co}(\text{NO}_3)_2 \cdot 6\text{H}_2\text{O}$, $\text{FeCl}_3 \cdot 6\text{H}_2\text{O}$, $\text{Ni}(\text{NO}_3)_2 \cdot 6\text{H}_2\text{O}$, *N,N*-dimethylformamide (DMF), terephthalic acid, PVP ($M_w = 40\,000$), methanol, ethanol, NaOH, and KOH were purchased from Sigma-Aldrich, Nafion solution (15 wt% in ethanol) was obtained from Ion Power. The deionized water used in this work was from a Millipore System.

Preparation of PVP-Functionalized $\text{Fe}_2\text{Ni_MIL-88}$: 0.3622 g $\text{FeCl}_3 \cdot 6\text{H}_2\text{O}$ and 0.192 g $\text{Ni}(\text{NO}_3)_2 \cdot 6\text{H}_2\text{O}$ were first dissolved in 20 mL DMF and then 0.3622 g terephthalic acid was added to the above solution with stirring until the solution became clear. After that, 4 mL 0.4 mol L^{-1} NaOH solution was then added for another 15 min of stirring. The obtained mixture was then transferred and sealed into a 50 mL Teflon-lined autoclave, and then hydrothermally reacted at 100 °C for 15 h. The yellow precipitate was collected by centrifugation and washed with DMF and ethanol for three times. Then the obtained product was ultrasonically dispersed into 60 mL methanol containing 3 g PVP ($M_w = 40\,000$) and followed with continuous stirring for 12 h. Then the PVP-functionalized product was collected and washed with methanol by centrifugation, and then redispersed in 45 mL methanol for further use.

Preparation of ZIF ZnCo: 4 mmol 2-methylimidazole was first dissolved in 50 mL methanol. Then a methanol solution containing 0.3 mmol $\text{Co}(\text{NO}_3)_2 \cdot 6\text{H}_2\text{O}$ and 0.3 mmol $\text{Zn}(\text{NO}_3)_2 \cdot 6\text{H}_2\text{O}$ was added to the above solution under vigorous stirring for 3–5 min. After that, the stirring was stopped, and the mixture was kept in static state for 24 h. Finally, the product was recovered and washed with methanol via centrifugation, followed by drying at 70 °C overnight.

Preparation of Fe₂Ni MIL-88@ZIF ZnCo: 4 mmol 2-methylimidazole was first dissolved in 50 mL methanol. 6 mL as-prepared PVP-functionalized Fe₂Ni MIL-88 solution was then added with vigorous stirring. Then a metal source of methanol solution containing 0.3 mmol Co(NO₃)₂·6H₂O and 0.3 mmol Zn(NO₃)₂·6H₂O was added to the obtained mixture stirring for 3–5 min and allowed to react for 24 h without stirring at room temperature. After that, a light pink product was recovered and washed with methanol via centrifugation for several times, then dried at 70 °C overnight.

Preparation of FeNiCo@NC: The Fe₂Ni MIL-88@ZIF ZnCo was pyrolyzed at a desirable temperature for 2 h with a ramp rate of 5 °C min⁻¹ in Ar atmosphere, then cooled to room temperature naturally.

Preparation of FeNiCo@NC-P: The as-prepared FeNiCo@NC and NaH₂PO₄ were put into two different porcelain boats. Both boats were placed closely at the middle of the furnace and keeping the boat containing NaH₂PO₄ on the upstream side. The tube furnace was then heated to 300 °C for 2 h with a ramp rate of 5 °C min⁻¹ with a slow rate of Ar flow.

Materials Characterization: The morphology and structure of as-prepared catalysts were characterized by field emission SEM (LEO FESEM 1350) and TEM (JEOL 2010F). The crystallite structure and phase of as-prepared catalysts were analyzed by XRD (MiniFlex 600, Rigaku). Nitrogen adsorption–desorption isotherms were measured at liquid nitrogen temperature by using the Micromeritics ASAP 2020 analyzer; the Brunauer–Emmett–Teller equation and the density functional theory model were used to determine the specific surface area and the pore size distribution, respectively. ICP test was conducted by using X Series 2, Thermo Scientific USA. The chemical compositions and states of as-prepared catalysts were investigated via XPS. The binding energy of samples was calibrated to fix the carbon sp³ peak at 284.6 eV.

Electrochemical Measurement: All catalysts were evaluated via a standard three-electrode system containing RDE, saturated calomel electrode (SCE), and graphite rod as working, reference, and counter electrodes on Biologic VSP-300 electrochemical workstation. The catalyst ink was prepared by blending 2 mg catalyst into 500 μL of 0.15 wt% Nafion ethanol solution. Then the ink was sonicated for 20 min and 40 μL ink was carefully dropped on the RDE (glassy carbon electrode for ORR test and gold electrode for OER test). All the measurements were conducted in 0.1 KOH solution and purged with O₂ or N₂ for 30 min based on the requirements of ORR and OER. ORR performance was investigated using CV and LSV techniques under different rotation speeds (400, 900, 1600, and 2500 rpm). The calculation of transferred electron number (*n*) of ORR was conducted based on the K–L equation

$$\frac{1}{j} = \frac{1}{j_L} + \frac{1}{j_K} = \frac{1}{B\omega^{1/2}} + \frac{1}{j_K} \quad (1)$$

$$B = 0.2nFC_0D_0^{2/3}\nu^{-1/6} \quad (2)$$

$$j_K = nFkC_0 \quad (3)$$

where *j* is the measured current density, *j_K* and *j_L* are the kinetic limiting and diffusion limiting current density, respectively, and ω is the electrode rotation rate (rad s⁻¹). *n* is transferred electron number, *F* is Faraday constant (96 485 C mol⁻¹), *C₀* is the bulk concentration of O₂, *D₀* is the diffusion coefficient of O₂, ν is the kinetic viscosity of the electrolyte, and *k* is the electron transfer rate constant. The constants adopted in the case of 0.1 M KOH at room temperature are as follow: *C₀* = 1.2 × 10⁻³ mol L⁻¹, *D₀* = 1.9 × 10⁻⁵ cm² s⁻¹, ν = 0.01 cm² s⁻¹. OER performance was measured from 0 to 0.8 V (vs SCE) with a scan rate of 10 mV s⁻¹ at 1600 rpm rotation. Commercial Pt/C (46.4 wt% Pt) and Ir/C (20 wt% Ir) were employed as benchmark materials for the ORR and OER tests, respectively. The potentials data presented in this work were calibrated to the reversible hydrogen electrode (RHE) based on the equation: *E_{RHE}* = *E_{SCE}* + 0.059 × pH + 0.241. The LSV of ORR and OER were calibrated by IR-compensation in 0.1 M KOH.

Zinc–Air Battery Test: In-house zinc–air batteries were assembled with polished zinc plate as anode and catalyst loaded carbon paper with gas diffusion layer (29 BC, Ion Power Inc). Copper foil and stainless steel meshes were used as current collectors for anode and cathode, respectively. The electrolyte for the batteries is a solution of 6 M KOH and 0.2 M ZnAc₂.

Supporting Information

Supporting Information is available from the Wiley Online Library or from the author.

Acknowledgements

D.R. and J.Y. contributed equally to this work. The authors acknowledge the financial support from the University of Waterloo and Wenzhou University, Natural Science and Engineering Research Council of Canada, (NSERC) National Natural Science Foundation of China (51872209 and 51772219), Zhejiang Provincial Natural Science Foundation of China (LZ17E02002), Part of the TEM work was performed at the Center for Functional Nanomaterials, Brookhaven National Laboratory, which was supported by the U.S. Department of Energy (DOE), Office of Basic Energy Science, under Contract No. DE-SC0012704.

Conflict of Interest

The authors declare no conflict of interest.

Keywords

bifunctional electrocatalyst, carbon nanotubes, metal–organic frameworks, transition metal phosphides, zinc–air batteries

Received: October 2, 2019
Revised: November 10, 2019
Published online:

- [1] a) N. Xu, Y. Zhang, T. Zhang, Y. Liu, J. Qiao, *Nano Energy* **2019**, *57*, 176; b) J. Fu, Z. P. Cano, M. G. Park, A. Yu, M. Fowler, Z. Chen, *Adv. Mater.* **2017**, *29*, 1702526.
- [2] M. Wu, Q. Wei, G. Zhang, J. Qiao, M. Wu, J. Zhang, Q. Gong, S. Sun, *Adv. Energy Mater.* **2018**, *8*, 1801836.
- [3] a) Q. Tang, L. Wang, M. Wu, N. Xu, L. Jiang, J. Qiao, *J. Power Sources* **2017**, *365*, 348; b) N. Xu, J. Qiao, Q. Nie, M. Wang, H. Xu, Y. Wang, X.-D. Zhou, *Catal. Today* **2018**, *318*, 144; c) J. Zhang, G. Jiang, T. Cumberland, P. Xu, Y. Wu, S. Delaat, A. Yu, Z. Chen, *InfoMat* **2019**, *1*, 234.
- [4] a) X. Li, F. Dong, N. Xu, T. Zhang, K. Li, J. Qiao, *ACS Appl. Mater. Interfaces* **2018**, *10*, 15591; b) L. Ma, S. Chen, Z. Pei, Y. Huang, G. Liang, F. Mo, Q. Yang, J. Su, Y. Gao, J. A. Zapien, C. Zhi, *ACS Nano* **2018**, *12*, 1949.
- [5] a) J. Park, M. Risch, G. Nam, M. Park, T. J. Shin, S. Park, M. G. Kim, Y. Shao-Horn, J. Cho, *Energy Environ. Sci.* **2017**, *10*, 129; b) Z. Zhang, Y. P. Deng, Z. Xing, D. Luo, S. Sy, Z. P. Cano, G. Liu, Y. Jiang, Z. Chen, *ACS Nano* **2019**, *13*, 7062; c) H. Jin, H. Huang, Y. He, X. Feng, S. Wang, L. Dai, J. Wang, *J. Am. Chem. Soc.* **2015**, *137*, 7588; d) C. Yang, H. Jin, C. Cui, J. Li, J. Wang, K. Amine, J. Lu, S. Wang, *Nano Energy* **2018**, *54*, 192.

- [6] a) H.-F. Wang, C. Tang, Q. Zhang, *Adv. Funct. Mater.* **2018**, *28*, 1803329; b) Y. Wang, L. Tao, Z. Xiao, R. Chen, Z. Jiang, S. Wang, *Adv. Funct. Mater.* **2018**, *28*, 1705356; c) T. Wang, G. Nam, Y. Jin, X. Wang, P. Ren, M. G. Kim, J. Liang, X. Wen, H. Jang, J. Han, Y. Huang, Q. Li, J. Cho, *Adv. Mater.* **2018**, *30*, 1800757; d) Y.-P. Deng, Y. Jiang, D. Luo, J. Fu, R. Liang, S. Cheng, Z. Bai, Y. Liu, W. Lei, L. Yang, J. Zhu, Z. Chen, *ACS Energy Lett.* **2017**, *2*, 2706.
- [7] a) S. Wang, C. M. McGuirk, A. d'Aquino, J. A. Mason, C. A. Mirkin, *Adv. Mater.* **2018**, *30*, 1800202; b) S. Fu, C. Zhu, J. Song, D. Du, Y. Lin, *Adv. Energy Mater.* **2017**, *7*, 1700363; c) S. Zheng, X. Li, B. Yan, Q. Hu, Y. Xu, X. Xiao, H. Xue, H. Pang, *Adv. Energy Mater.* **2017**, *7*, 1602733; d) B. Y. Guan, L. Yu, X. W. Lou, *Energy Environ. Sci.* **2016**, *9*, 3092; e) T. Wang, Z. Kou, S. Mu, J. Liu, D. He, I. S. Amiinu, W. Meng, K. Zhou, Z. Luo, S. Chaemchuen, F. Verpoort, *Adv. Funct. Mater.* **2018**, *28*, 1705048; f) H. Zhang, Z. Yang, X. Wang, S. Yan, T. Zhou, C. Zhang, S. G. Telfer, S. Liu, *Nanoscale* **2019**, *11*, 17384; g) X. F. Lu, Y. Chen, S. Wang, S. Gao, X. W. D. Lou, *Adv. Mater.* **2019**, *31*, 1902339; h) X. D. Lou, *Angew. Chem., Int. Ed.* **2019**, <https://doi.org/10.1002/anie.201910309>.
- [8] S. Bhattacharyya, C. Das, T. K. Maji, *RSC Adv.* **2018**, *8*, 26728.
- [9] a) Z. Peng, D. Jia, A. M. Al-Enizi, A. A. Elzatahry, G. Zheng, *Adv. Energy Mater.* **2015**, *5*, 1402031; b) L. Zeng, X. Cui, L. Chen, T. Ye, W. Huang, R. Ma, X. Zhang, J. Shi, *Carbon* **2017**, *114*, 347; c) Y. Feng, C. Xu, E. Hu, B. Xia, J. Ning, C. Zheng, Y. Zhong, Z. Zhang, Y. Hu, *J. Mater. Chem. A* **2018**, *6*, 14103; d) C. Li, M. Wu, R. Liu, *Appl. Catal., B* **2019**, *244*, 150; e) J. Zhu, M. Xiao, Y. Zhang, Z. Jin, Z. Peng, C. Liu, S. Chen, J. Ge, W. Xing, *ACS Catal.* **2016**, *6*, 6335.
- [10] a) S. Gupta, L. Qiao, S. Zhao, H. Xu, Y. Lin, S. V. Devaguptapu, X. Wang, M. T. Swihart, G. Wu, *Adv. Energy Mater.* **2016**, *6*, 1601198; b) G. Nam, Y. Son, S. O. Park, W. C. Jeon, H. Jang, J. Park, S. Chae, Y. Yoo, J. Ryu, M. G. Kim, S. K. Kwak, J. Cho, *Adv. Mater.* **2018**, *30*, 1803372.
- [11] G. Huang, F. Zhang, L. Zhang, X. Du, J. Wang, L. Wang, *J. Mater. Chem. A* **2014**, *2*, 8048.
- [12] W. Xia, J. Zhu, W. Guo, L. An, D. Xia, R. Zou, *J. Mater. Chem. A* **2014**, *2*, 11606.
- [13] a) K. Ai, Z. Li, X. Cui, *J. Power Sources* **2017**, *368*, 46; b) W. Sun, X. Zhai, L. Zhao, *Chem. Eng. J.* **2016**, *289*, 59.
- [14] A. Aijaz, J. Masa, C. Rosler, W. Xia, P. Weide, A. J. Botz, R. A. Fischer, W. Schuhmann, M. Muhler, *Angew. Chem., Int. Ed.* **2016**, *55*, 4087.
- [15] J. Fu, F. M. Hassan, J. Li, D. U. Lee, A. R. Ghannoum, G. Lui, M. A. Hoque, Z. Chen, *Adv. Mater.* **2016**, *28*, 6421.
- [16] X. Wang, W. Ma, Z. Xu, H. Wang, W. Fan, X. Zong, C. Li, *Nano Energy* **2018**, *48*, 500.
- [17] Z. Wang, Y. Dong, H. Li, Z. Zhao, H. B. Wu, C. Hao, S. Liu, J. Qiu, X. W. Lou, *Nat. Commun.* **2014**, *5*, 5002.
- [18] Z. Y. Wu, X. X. Xu, B. C. Hu, H. W. Liang, Y. Lin, L. F. Chen, S. H. Yu, *Angew. Chem., Int. Ed.* **2015**, *54*, 8179.
- [19] M. Wu, Q. Tang, F. Dong, Y. Wang, D. Li, Q. Guo, Y. Liu, J. Qiao, *Phys. Chem. Chem. Phys.* **2016**, *18*, 18665.
- [20] a) M. Wang, T. Qian, J. Zhou, C. Yan, *ACS Appl. Mater. Interfaces* **2017**, *9*, 5213; b) J. S. Li, S. L. Li, Y. J. Tang, M. Han, Z. H. Dai, J. C. Bao, Y. Q. Lan, *Chem. Commun.* **2015**, *51*, 2710.
- [21] Y. Hao, Y. Xu, W. Liu, X. Sun, *Mater. Horiz.* **2018**, *5*, 108.
- [22] a) Z.-H. Xue, H. Su, Q.-Y. Yu, B. Zhang, H.-H. Wang, X.-H. Li, J.-S. Chen, *Adv. Energy Mater.* **2017**, *7*, 1602355; b) R. Tang, C. Jiang, W. Qian, J. Jian, X. Zhang, H. Wang, H. Yang, *Sci. Rep.* **2015**, *5*, 13645.
- [23] K. Chen, X. Huang, C. Wan, H. Liu, *Chem. Commun.* **2015**, *51*, 7891.
- [24] X. Li, Q. Jiang, S. Dou, L. Deng, J. Huo, S. Wang, *J. Mater. Chem. A* **2016**, *4*, 15836.
- [25] S. H. Ahn, A. Manthiram, *Small* **2017**, *13*, 1702068.
- [26] T. Liu, K. Wang, G. Du, A. M. Asiri, X. Sun, *J. Mater. Chem. A* **2016**, *4*, 13053.
- [27] C. Lin, Z. Gao, J. Yang, B. Liu, J. Jin, *J. Mater. Chem. A* **2018**, *6*, 6387.
- [28] H. Lei, M. Chen, Z. Liang, C. Liu, W. Zhang, R. Cao, *Catal. Sci. Technol.* **2018**, *8*, 2289.
- [29] S. Liu, Z. Wang, S. Zhou, F. Yu, M. Yu, C. Y. Chiang, W. Zhou, J. Zhao, J. Qiu, *Adv. Mater.* **2017**, *29*, 1700874.
- [30] J. Meng, C. Niu, L. Xu, J. Li, X. Liu, X. Wang, Y. Wu, X. Xu, W. Chen, Q. Li, Z. Zhu, D. Zhao, L. Mai, *J. Am. Chem. Soc.* **2017**, *139*, 8212.
- [31] a) W. Liu, J. Zhang, Z. Bai, G. Jiang, M. Li, K. Feng, L. Yang, Y. Ding, T. Yu, Z. Chen, A. Yu, *Adv. Funct. Mater.* **2018**, *28*, 1706675; b) K. J. J. Mayrhofer, D. Strmcnik, B. B. Blizanac, V. Stamenkovic, M. Arenz, N. M. Markovic, *Electrochim. Acta* **2008**, *53*, 3181; c) Q. Liu, J. Jin, J. Zhang, *ACS Appl. Mater. Interfaces* **2013**, *5*, 5002.